Batteries & Supercaps

Research Article
doi.org/10.1002/batt.202300149

Chemistry Europe
European Chemical Societies Publishing

www.batteries-supercaps.org

A Long Cycle Life Zinc-Iodide Flow Battery Enabled by a Multifunctional Low Cost Supporting Electrolyte

Monalisa Chakraborty,[a, b] Teresa Andreu,*[c, d] Maxim Guc,[a] Mohamed Amazian,[c] and Sebastián Murcia-López*[a]

High energy density and cost-effective zinc-iodide flow battery (ZIFB) offers great promise for future grid-scale energy storage. However, its practical performance is hindered by poor cyclability, because of irreversible zinc plating/stripping, slow kinetics of redox reactions, and solid I_2 precipitation. Herein, we report NaCl-supported electrolyte chemistry to address these issues simultaneously. The formation of soluble chloride anions by coordination interactions between Zn^{2+} and Cl^-, are key factor for the improvement of Zn/Zn^{2+} redox reversibility. While formation of soluble I_2Cl^- complex stabilizes ZIFB from I_2 precipitation, participation of Na^+ and K^+ as dominant migrating carriers passing through Nafion, restricts Zn^{2+} migration, thus, blocking electrolyte crossover. A ZIFB with this improved electrolyte stably cycled 100 times with excellent capacity retention and energy efficiency at 20 mA cm^{-2}, while conventional ZIFB shows the trend of capacity fade from 10th cycle onwards. These encouraging results of NaCl-added electrolyte chemistry enlighten great prospects for high-performance ZIFB applications.

Introduction

The increasing utilization of renewable but intermittent energy sources such as solar and wind causes great concern about the performance and reliability of the electrical grid infrastructure.[1] Large-scale energy storage systems are regarded as a crucial solution in improving grid reliability and power quality.[2–7] Particularly, redox flow batteries (RFBs) have attracted wide interest among various electrochemical energy storage systems, thanks to their unique features of design flexibility, excellent scalability, and short response time.[4,8–12] To date, various redox flow battery chemistries[13–16] have been proposed including mostly investigated all-vanadium,[17–19] iron-chromium,[20,21] and zinc bromine,[22–24] but none of them significantly penetrated the marketplace due to several limitations such as low energy density, limited cycle life and high cost.[4,14,24–26] Therefore, it is an urgent need to develop next generations RFBs using highly soluble, inexpensive, and environment-friendly redox-active materials to meet the high energy density criteria as well as reduce the total cost. Among various undergoing investigations of developing new RFB chemistries, zinc-iodide RFB has attracted gross attention due to the utilization of earth-abundant zinc as an active material which provides two electrons in each half-cell reaction, thus achieving higher energy density, as well as using highly-soluble zinc iodide (ZnI_2) as both electrolytes.[1,27–31] Although promising, several challenges must be addressed before the successful advancement, such as poor cyclability as a consequence of capacity fading over cycling which is mainly due to the irreversible Zn plating/stripping and insoluble solid I_2 precipitation. Also, the low electrolyte conductivity and slow kinetics of redox reactions result in low operating current density, voltage, and energy efficiency.[32,33] Weng et al. reported a ZIFB by the introduction of Br^- ions in the electrolyte as a complexing agent to stabilize I_2 molecules and free up the I^- ions, which leads to increased capacity; however, low operating current density (~5–10 mA cm^{-2}) and zinc dendrite growth on anode decays the cycling performance.[28] Investigations have been done on various organic and inorganic electrolyte additives to suppress the Zn dendrite.[34–36] For example, Li et al. employed ethanol as the additive in ZIFB to ameliorate the Zn dendrite growth by ligand formation between oxygen and Zn^{2+} ions which promotes a smoother Zn deposition. However, the addition of organic molecules decreases the ion conductivity of the electrolyte resulting in lower energy efficiency (EE).[27,36] On the other side, Zn complex formation with inorganic NH_4^+ ions holds great promise so far.[31,37] Jian et al. demonstrated the improvement of electrochemical performance of ZIFB with NH_4Br as a supporting electrolyte by mitigating Zn dendrite formation due to $Zn(NH_3)_x^{2+}$ complexation effect.[31] Goh et al. explained the improvement of the reversibility of the Zn anode in the neutral Zn-air batteries because of the complexation effects of NH_4^+ and Zn^{2+} ions.[37]

[a] Dr. M. Chakraborty, Dr. M. Guc, Dr. S. Murcia-López
Catalonia Institute for Energy Research (IREC)
Jardins de les Dones de Negre 1, Sant Adrià de Besós, 08930, Spain
E-mail: smurcia@irec.cat
[b] Dr. M. Chakraborty
Universitat Autonoa de Barcelona (UAB)
Plaça Cívica, Bellaterra, 08193, Spain
[c] Dr. T. Andreu, M. Amazian
Universitat de Barcelona (UB)
Martí i Franqus 1, Barcelona, 08028, Spain
E-mail: tandreu@ub.edu
[d] Dr. T. Andreu
Institut de Nanciència i Nanotecnologia (IN2UB)
Martí i Franquès 1, Barcelona, 08028, Spain

Supporting information for this article is available on the WWW under https://doi.org/10.1002/batt.202300149

Research Article
doi.org/10.1002/batt.202300149
Chemistry Europe
European Chemical Societies Publishing

In this work, we propose a ZIFB with improved electrolyte incorporating cost-effective NaCl as a supporting electrolyte to enhance the cell performance by addressing the above-discussed issues. The electrochemical and physicochemical characterization reveal the improvement of Zn/Zn^{2+} redox reversibility due to the complexation interactions between Zn^{2+} and Cl^- in the formation of $ZnCl_4^{2-}$ anions, while stabilization of I_2 by complexation with Cl^-, and participation of monovalent Na^+ as another main migrating cation through the cation exchange membrane (CEM) in catholyte solution chemistry. As a result, the ZIFB employing NaCl-added electrolyte delivers highly stable coulombic efficiencies for 100 cycles with exceptionally reversible Zn plating and stripping on the anode.

Results and Discussion

Half-cell electrochemical performance

CV tests were firstly investigated between the scan rates 10 to 50 $mV\,s^{-1}$, to understand the effects of NaCl as a supporting electrolyte on the electrochemical performance of both Zn/Zn^{2+} and I_3^-/I^- redox reactions. Figure 1(a) shows the CV curve of Zn/Zn^{2+} redox reactions in electrolytes with and without Cl^- ions. It is seen that the solid Zn began depositing at the surface of the working electrode (GCE) at approximately −1.55 to −1.6 V (vs. Hg/Hg_2SO_4) at all scan rates in electrolyte without NaCl. In the reverse scan, the anodic peak position, which corresponds to the Zn^{2+} stripping (oxidation reaction) from the anode, shows a clear difference in peak shifting of the electrolytes without and with NaCl. The peak appears at approximately −1.3 V (vs. Hg/Hg_2SO_4) with a negligible shifting in the further scan rates with the electrolyte with Cl^- ions, whereas much positive shifting has been observed in the solution without NaCl. Moreover, it is interesting to mention that overall, the reductive and oxidative peaks separation is significantly lower with the introduction of Cl^- ions, by shifting the reductive and oxidative peaks towards positive and negative potentials respectively, which depicts the enhanced reversibility of Zn plating and stripping. The total peak separation (ΔE_p) vs. logarithm of scan rates (Figure S1a) curves summarize the above-discussed observations. On the other hand, Figure 1(b) displays the CV results of I_3^-/I^- redox reaction. It is evident that the introduction of NaCl in the electrolyte significantly decreases the overpotentials of both oxidation and reduction, respectively. As a result, the anodic and cathodic peak potential difference (ΔE_p) reduces substantially (Figure S1b). Moreover, the oxidation and reduction peak currents are higher than those in the pristine solution, and also exhibit a linear dependence on the square root of scan rates (Figure S1c), implying that the I_3^-/I^- redox reaction rate is diffusion-limited. The comparison of diffusion coefficients of I^- and I_3^-, calculated based on Randles-Sevcik equation (table S1) presents an eye-catching enhancement in the presence of NaCl. To sum up, the presence of NaCl as a supporting electrolyte is beneficial in both, anode and cathode sides redox reactions in terms of reversibility, by showing lower anodic and cathodic polarization as well as improvement in the kinetics of I_3^-/I^- redox reaction via enhancement of diffusion coefficients. Therefore, these CV results could provide strong evidence that adopting NaCl as a supporting electrolyte is helpful for the electrochemical performance of ZIFB.

Electrochemical performance of ZIFB

To investigate the effect of NaCl supporting electrolyte on the full cell cycling performance, ZIFB single cells were assembled to perform the traditional galvanostatic cycling at a current density of 20 $mA\,cm^{-2}$. Figure 2(a) displays the cycling efficiencies of cells assembled with and without NaCl. A sudden drop in the coulombic efficiency (CE) and discharge capacity (Figure 2b) after few cycles is observed in the cell without NaCl in the electrolyte, which follows a continuous degradation of CE. Moreover, the representation of capacity retention with cycling (Figure 2b) displays a clear image of dramatic capacity loss throughout the cycling. The optical image of cycled anode after disassembling the cell in Figure 2(c) shows that a high amount of Zn deposition remained on the electrode, which enlightens

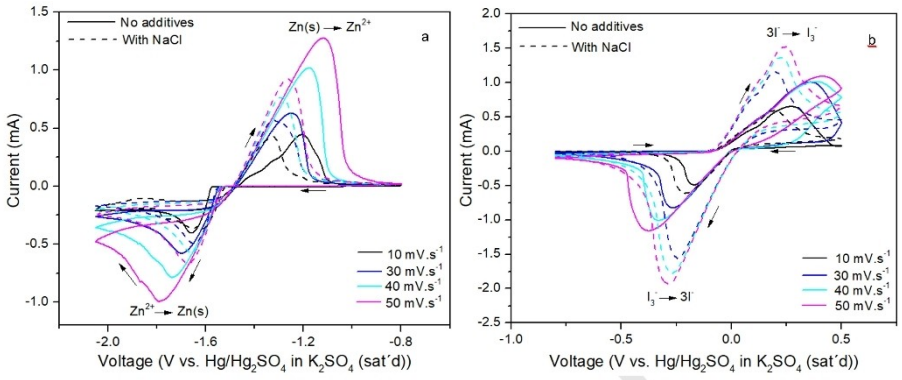

Figure 1. Cyclic voltammograms of a) Zn/Zn^{2+} redox reaction, and b) I_3^-/I^- redox reaction at the scan rates between 10–50 $mV\,s^{-1}$ in 25 mM ZnI_2:KI with and without NaCl.

Research Article
doi.org/10.1002/batt.202300149
Chemistry Europe
European Chemical Societies Publishing

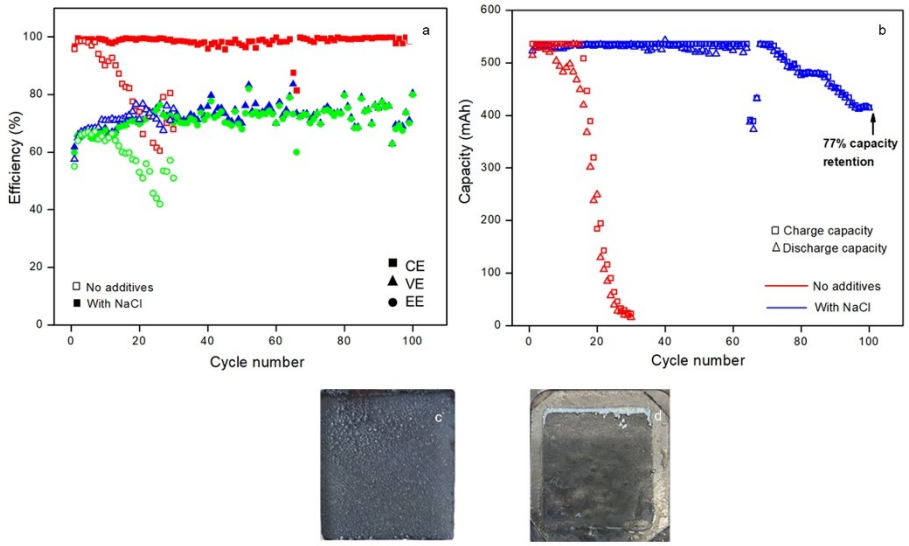

Figure 2. Comparison of cycling performances of ZIFB with and without NaCl at a current density of 20 mA cm^{-2}. a) Coulombic, voltage, and energy efficiencies, b) charge-discharge capacity; optical images of post-cycled anodes c) without NaCl, after 30 cycles and d) with NaCl, after 100 cycles.

the reason for capacity degradation. The voltage profile of the cell cycled at 40 mA cm^{-2} (Figure S2b) exhibits a high polarization loss. In contrast, the battery with NaCl media could be cycled stably for 100 cycles without significant capacity decay and 77% capacity retention at the end of 100 cycles, which finally does not affect the excellent EE. The voltage profile (Figure S2a) demonstrates stable behaviour, almost all the curves overlap with each other, suggesting decent cycling stability of the battery in the presence of NaCl. After certain long cycling (from the 70th cycle onwards), the charge and discharge capacity of the battery experienced a slow decrease (also could be seen in the charge-discharge curve of the 100th cycle in Figure S2a), which might be ascribed to either unavoidable losses during the long cycling associated to crossover of active species through the membrane or due to some electrodeposited Zn partially came off but possibly not in completely irreversible manner which reflects in the recovering of CE after sudden drop between 70th–72nd cycles (Figure 2a). Most possibly, electrodeposited Zn dissolved back because of highly soluble complex forming nature of NaCl with Zn, still not so reversible way, thus, charge capacity degradation occurred in later cycling as a result of concentration gradient in the solution. As shown in the photograph in Figure 2(d), the anode of the cell cycled in the presence of NaCl unveils that no Zn remains on the electrode, proving improved stability and reversibility of the Zn plating/stripping process in the NaCl media. The small accumulation in the top part of the electrode can be attributed to the effect of a non-favourable fluid hydrodynamics at the vicinity of the sealing gasket. Furthermore, the voltage profile at 40 mA cm^{-2} (Figure S2b) suggests stable and well-coincided curves with each other upon repeated cycling along with lower polarization loss compared to the battery cycled without NaCl. The enhancement of the discharge voltage of the battery with NaCl-containing electrolyte can be seen in the discharge polarization and power density curves (Figure S3), which exhibit an increment of the peak power density of 36 mW cm^{-2} the maximum current density of 60 mA cm^{-2}. To sum up, these results confirm that NaCl is an effective supporting electrolyte for offering reversible Zn plating and stripping, thus improving the cyclability of ZIFB.

Effect of NaCl as an additive on the anode side

For assessing the role of NaCl in the efficient Zn plating in a half-cell mode, the characterization of electrodeposited Zn on planar FTO substrate has been performed. Figure 3 represents the SEM images of cross-sectional morphology and thickness of electrodeposited Zn after a charge for 90 min at 20 mA cm^{-2} with the pristine and NaCl added electrolyte, respectively.

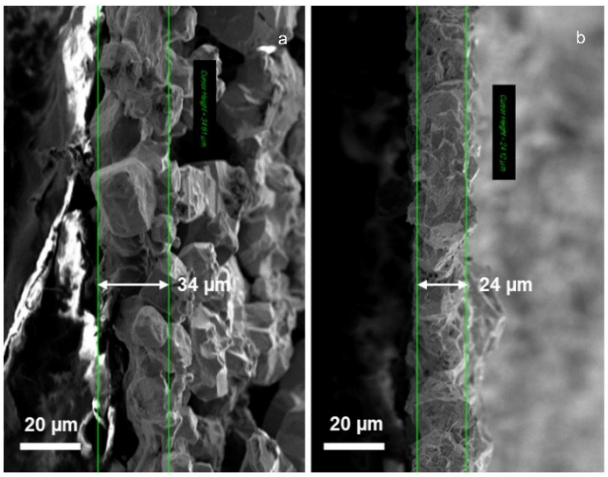

Figure 3. Cross-sectional morphologies of Zn deposited on FTO substrate at 20 mA cm^{-2} with an areal capacity of 30 mAh cm^{-2} in 1.5 M ZnI_2:KI electrolyte of a) without and, b) with 1.5 M NaCl.

Research Article
doi.org/10.1002/batt.202300149
Chemistry Europe
European Chemical Societies Publishing

These images depict that the Zn deposition with the NaCl supported electrolyte is compact and densely packed, showing lower thickness compared to the deposition of larger size of clusters in the case of pristine electrolyte. The mass of the deposition corresponding to the total applied charge is further validated by the theoretical calculation based on Faraday's law (in supporting information) and it shows a very close value to the actual weight of the Zn deposition in NaCl supported electrolyte. This denser and more packed pattern of Zn deposition morphology by the introduction of Cl^- ions have also been reported in previous studies.[39–41] Additionally, XRD patterns of deposited Zn on graphite foil substrate in the electrolyte with and without NaCl (Figure S4) depict only metallic Zn (JCPDS 004-0831) without any impurities along with a peak of weak intensity, which belong to the graphite (JCPDS041-1487). For both electrolytes, deposited Zn belongs to the hexagonal crystalline group and exhibits a certain predominant orientation towards the [101] reflection plane. The average crystallite sizes of the Zn deposition, estimated from the FWHM of the [101] plane using Scherrer's formula are 115 and 72 nm of electrolyte without and with NaCl, respectively. This lower crystallite size in the presence of Cl^- ions justifies the densely packed elemental Zn, while the more intense graphite peak observed from the graphite foil substrate justify the thinner Zn layer, observed in the SEM image.

As a quick summary of the results, we have pointed out so far that introduction of NaCl leads to significant improvements in the electrochemical performance of Zn/Zn^{2+} half-cell. For instance, the CV results have revealed that NaCl enhances the reversibility of Zn/Zn^{2+} redox reactions, which further reflects through the excellent cyclability and capacity retention in the ZIFB cycling, following reversible Zn plating/de-plating on the anode. Moreover, Cl^- ions in the electrolyte facilitate a smooth, densely packed, and properly oriented Zn plating on the anode.

Next, to better interpret the equilibrium chemistry of these two electrolytes, chemical equilibrium diagrams were calculated using the Hydra-Medusa software and equilibrium database. Figure S5 shows the distribution of zinc species as a function of pH in the two anolytes of without and with NaCl, when total concentrations of ion are $[Zn^{2+}] = 1.5\ mol\,L^{-1}$, $[I^-] = 4.5\ mol\,L^{-1}$ and $[Cl^-] = 1.5\ mol\,L^{-1}$, respectively. It is found that the amount of free Zn^{2+} decreases with the introduction of Cl^- ions in the solution, as a large number of zinc species consisting of $ZnCl_x^{(2-x)}$ ($x = 1, 2, 3, 4$) appear in the NaCl added electrolyte between pH range from 1 to 6 (Figure S5b). These results of forming soluble chloride salts within these lower pH ranges are in good agreement with the previously reported literatures on zinc-chloride media.[40,42–44] In fact, correlation of Zn morphology, crystal size, nucleation mode and concentration of Zn^{2+} and Cl^- species has been addressed in literature concerning Zn electroplating.[40] An instantaneous nucleation mechanism is dominant under Zn^{2+} and Cl^- concentrations above certain critical values, leading to formation of denser and more compact layers, as those observed by us.

For practical insights into the functionality of Cl^- ions in the solution chemistry, the electrolyte solutions, with and without NaCl, were studied by Raman spectroscopy. As illustrated in Figure 4, the Raman spectrum of the solution, without NaCl contains three distinctive bands at 122, 138, and 164 cm^{-1} respectively. These three bands observed are in good agreement with the previous works reported in the literature,[27,45] and can be assigned to the A1 symmetry modes, which correspond to the symmetric stretching vibrations of the $[ZnI_4]^{2-}$, $[ZnI_3]^-$ and $[ZnI_2]$ complexes, respectively. Additionally, a shoulder at 178 cm^{-1} can be assigned to the T_2 symmetry mode of the $[ZnI_4]^{2-}$ complex.[45] The addition of NaCl in the solution leads to the appearance of a new peak at 281 cm^{-1} which can be assigned to the stretching mode of $[ZnCl_4]^{2-}$ complex.[46] This correlates with the significant decrease in the intensity of the peak associated to the $[ZnI_4]^{2-}$ complex in relation to the other peaks, allowing us to conclude that namely inside this complex chloride substitutes iodide. Additionally, the peak related to the $[ZnI_2]$ complex shifts to the lower energies to 158 cm^{-1} in the Cl^- media, which might be related to the influence of the Cl atoms, and the appearance of more complex Cl^--I^- vibrations. Overall, this comparison of Raman spectra of NaCl based electrolyte with the standard electrolyte confirms the coordination interactions between Zn^{2+} and Cl^- ions results in the formation of $ZnCl_4^{2-}$ anions.

Besides the chemical analysis, EIS tests at OCV on two-electrode configuration with graphite foil as working electrode were conducted before and after Zn electroplating. As depicted in the Nyquist plots in figure S6, series resistance values in the range of 2.1–2.3 Ω were observed in all the cases, using electrolytes with and without NaCl. These results suggest that the addition of extra NaCl does not have a significant effect on the electrical conductivity.

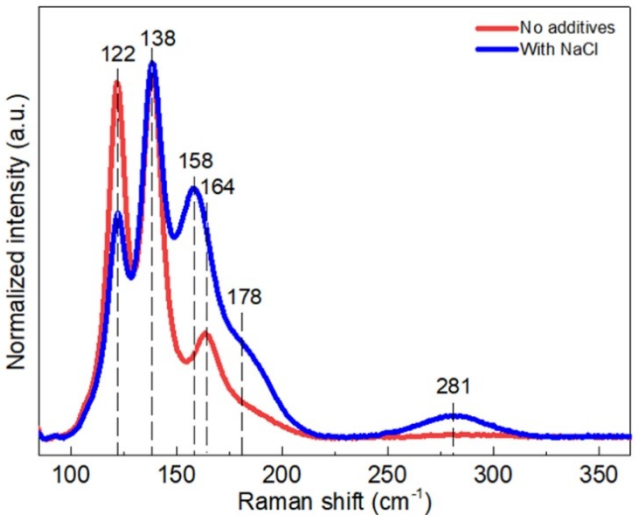

Figure 4. Raman spectroscopic investigation of electrolyte of 1.5 M ZnI_2:KI (at 0% SOC), red and blue colour represents electrolyte composition without and with 1.5 M NaCl supporting electrolyte.

Effect of NaCl as an additive on the cathode side

Apart from the improvements in the electrochemical performance of Zn/Zn^{2+} half-cell by the introduction of NaCl, in parallel, CV results also reveal the enhancements of I_3^-/I^- redox reaction in terms of kinetics and reversibility. Hence, to understand the role of Cl^- ions in the solution chemistry of cathode half-cell, Raman spectroscopy was performed of fully charged catholyte (67% SoC), without and with NaCl (Figure S7). As shown in the Raman spectrum of NaCl free electrolyte, two intense bands related to the polyiodides appear at 111 and 156 cm^{-1}, which can be assigned to the symmetric stretch of triiodide (I_3^-) and outer symmetric stretch of pentaiodide (I_5^-), respectively.[27,47] Besides, a weak band appears at 235 cm^{-1}, attributed to the polyiodide species. With the addition of NaCl to the solution, a new band appears at 230 cm^{-1} which represents the formation of the soluble I_2Cl^- complex in the catholyte. This result of the formation of I_2Cl^- complex is in good agreement with the report published by M. Mousavi et al.[48] This observation agrees with the statement made by M. Mousavi et al, about the stabilization of free iodine and freeing up the I^- ions by the formation of I_2Cl^-[48] and I_2Br^-[28] complexes during charging. In fact, other interhalide species such as ICl and $[ICl_2]^-$ have been identified to be electrochemically formed in mixed I^- and Cl^- systems, although at higher $[Cl^-]/[I^-]$ ratios.[49] Moreover, chemical equilibrium diagrams were calculated to obtain the distribution of I^- species as a function of pH in the catholytes containing without and with NaCl (Figure S8).

Formation of I_2Cl^- complex and availability of more free I^- ions has been observed with the NaCl-supported catholyte (Figure S8d), adding another parallel justification. Finally, this Cl^- ions complexation with I_2, hinders I_2 precipitation thus enhancing the ZIFB performance by withholding the battery capacity and CE (Figure 2a & b).

In another angle, this observed excellent and stable coulombic efficiency of the ZIFB with NaCl supported electrolyte (Figure 2a) can also be associated to the preferential monovalent cation transfer across the N117 CEM. In fact, the volume comparison between the cycled and fresh catholytes (Figure S9) shows no change of volume with NaCl-based catholyte even after 100 cycles, whereas a decrement has observed in the NaCl-free catholyte. Water transport is associated to cation diffusion along the ionic exchange membrane. As summarized in literature, divalent cations such as Zn^{2+} ions, possesses higher charge density, hydration enthalpy and water uptake capacity, therefore carrying more water molecules through the membrane. Although these divalent cations have lower self-diffusion coefficient and lower mobility than monovalent cations such as K^+ and Na^+,[50–53] in the absence of NaCl, after initial diffusion of K^+ through the N117 CEM, Zn^{2+} are prone to transfer from catholyte to anolyte, in order to compensate differences in the ionic strength. In the presence of NaCl, the K^+ and Na^+ are the dominant migrating carriers through the membrane, thus, restricting the mobility of Zn^{2+} and the water transfer from catholyte to anolyte, thus suppressing volume imbalance during cycling. This explanation adds another angle of positive impact of NaCl based solution chemistry in the long term ZIFB cycling with excellent capacity retention.

On a final note, this ZIFB with NaCl based solution chemistry outperformed the cyclability of conventional ZIFB system.[27] In fact, to our knowledge among the classical redox flow battery format of using traditional Nafion CEM, same electrolytes in the both sides without introducing organic-based or corrosive bromine-based supporting electrolytes, this NaCl supported ZIFB demonstrated the highest discharge energy density of 57.0 Wh L^{-1} at 20 mA cm^{-2} (see comparative table of various ZIFBs reported so far in Table S2). Moreover, maintaining the classical flow battery design provides the room for future research direction in ZIFBs of enhancing the energy density with higher electrolyte concentrations.

Conclusions

In summary, NaCl is proposed as an effective supporting electrolyte for ZIFBs long-term cycling. Inspired by the CV results of improved redox reversibility of Zn/Zn^{2+} in the presence of Cl^- ions, accordingly, this electrolyte enables the ZIFB to achieve a stable cycling performance for 100 cycles with 77% of capacity retention, along with highly reversible Zn plating and stripping. In addition, SEM image and XRD results reveal the densely packed morphology of Zn plating in the presence of Cl^- ions. Moreover, prediction of the coordination interactions between Zn^{2+} and Cl^- ions by chemical equilibrium diagrams, further confirmed by Raman spectroscopy and proves the formation of soluble, $ZnCl_4^{2-}$ anions, which are responsible for stabilization of Zn^{2+}, hence improving the Zn/Zn^{2+} redox electrochemical reaction. On the positive half-cell side, Cl^- ions complexation with I_2, frees up the I^- ions and blocks solid I_2 precipitation thus enhancing the ZIFB performance by retaining the battery capacity. Last but not the least, participation of Na^+ ions in catholyte solution chemistry, restricts the mobility of large, hydrated Zn^{2+}, thus blocking water migration from catholyte to anolyte by showing no volume change after 100 cycles, greatly reflects on the excellent capacity retention throughout the cycling.

Experimental Section

Electrolyte preparation

Zinc iodide (ZnI_2, $\geq$98%, Aldrich), potassium iodide (KI, $\geq$99.5%, Merck), and sodium chloride (NaCl, $\geq$99%, Sigma Aldrich) were used as purchased without further purification. 1.5 M ZnI_2 and KI (1:1) in deionized water (milli-Q ultrapure water) were used as the standard electrolyte. Catholyte solution was prepared by adding 2 M of KI extra into the standard electrolyte 1.5 M ZnI_2 and KI (1:1) for mass balance between compartments. When required, 1.5 M NaCl was added to the electrolyte on both sides. All the solutions were prepared at room temperature.

Assembly of lab-scale ZIFB

The assembling of ZIFB single cell was described in detail in our previous publication.[38] Electrodes of 10 cm^2 geometric area were assembled by sandwiching a commercial Nafion® 117 membrane between anode and cathode compartments. N117 underwent a pre-treatment in the following solutions: 3% H_2O_2, deionized water, and 0.5 M H_2SO_4 at 80 °C for 1 hour in each respectively. Graphite foil (Alfa Aesar®, 0.5 mm thick) and graphite felt (Sigracell® GFA 1.5 EA, 1.5 mm thick) were used as anode and cathode respectively. Graphite felt was thermally treated at 420 °C for 10 hours in an air atmosphere with a ramp rate of 5 °C min^{-1}. A titanium metal plate was used as a negative current collector. Around 4 mm space was kept between the anode surface and membrane for the metallic Zn plating. A graphite plate was used as a positive current collector. Electrolyte volume of 10 mL each, was circulated to the cell by a peristaltic pump (Masterflex L/S series) through Tygon® tubing at a fixed flow rate of 25 mL min^{-1}.

Electrochemical characterization

Cyclic voltammogram (CV) tests were carried out in a conventional three-electrode cell. A static glassy carbon electrode (GCE) with a diameter of 3 mm was used as working electrode while a Hg/Hg_2SO_4 in K_2SO_4 solution (saturated) and platinum mesh served as the reference and counter electrodes, respectively. 25 mM solution (ZnI_2:KI) in the presence or absence of 25 mM NaCl was used for the CV test at the scan rate ranging between 10 to 50 mV s^{-1}. On the negative side half-cell, a potential sweep between −0.8 V to −2.05 V vs Hg/Hg_2SO_4 (forward and reverse scan) was carried out to reduce Zn^{2+} and oxidize metallic Zn (s) at the surface of the GCE. On the positive side half-cell, forward and reverse sweep was carried out between −0.8 V to 0.5 V vs Hg/Hg_2SO_4 to oxidize I^- and reduce I_3^- respectively. The diffusion coefficient associated with I^- oxidation and I_3^- reduction reactions were calculated by applying the Randles-Sevcik method as per Equation (1):

$$i_p = 0.4463\ nFAc_0\left(\frac{nF\nu D}{RT}\right)^{\frac{1}{2}} \quad (1)$$

where i_p is peak current (A), F is Faraday constant (C mol^{-1}), T is temperature (K), n is the number of electrons ($n=2$), A is the electrode surface area (0.07 cm^2), c_0 is the bulk concentration of active species (mol L^{-1}), ν is the scan rate (v s^{-1}) and D is the diffusion coefficient (cm^2 s^{-1}). Using the slopes of the fitted linear Randles-Sevcik plots, diffusion coefficient was calculated.

Electrochemical impedance spectroscopy (EIS) measurements were conducted in a two-electrode connection within a frequency range of 200 kHz to 100 mHz and 10 mV of AC perturbation. EIS was measured at open-circuit conditions before and after metallic zinc electroplating (225 C cm^{-2} of total charge was applied at a current density of 20 mA cm^{-2}) on a graphite foil working electrode.

The zinc electrodeposition tests were done in a two-electrode electrochemical cell using FTO (Aldrich, surface resistivity of ~13 Ω sq^{-1}) of 1 cm^2 area as working and platinum mesh as counter electrodes respectively. Galvanostatic deposition at a current density of 20 mA cm^{-2} was carried out up to 54 C cm^{-2} of total charge was applied.

The charge-discharge cycles of ZIFB were operated under galvanostatic conditions at 20 and 40 mA cm^{-2}. The charge was controlled by upper cut-off voltage (1.7 V) and 67% of theoretical capacity (~54 Ah L^{-1}). The reason for choosing 67% of theoretical capacity was discussed in detail in our previous publication.[38] And discharge was controlled by lower cut-off voltage (0.3 V). Coulombic (CE), voltage (VE) and energy (EE) efficiencies were calculated by Equations (2)–(4), where Q is the battery capacity and V is the average cell potential during the charge/discharge.

$$CE = \frac{Q_{discharge}}{Q_{charge}} \quad (2)$$

$$VE = \frac{V_{discharge}}{V_{charge}} \quad (3)$$

$$EE = CE \times VE \quad (4)$$

All the experiments were carried out using an electrochemical workstation (Biologic® VMP3 potentiostat) at room temperature (~25 °C).

Physicochemical characterization

The thickness of the solid zinc layer was observed using a Zeiss Auriga 60 field emission scanning electron microscope (FE-SEM) with an acceleration voltage of 5 kV. The crystalline structures of deposited zinc were characterized by X-ray diffraction (XRD) using a Bruker D8 Advance diffractometer with Ni filtered Cu K_α radiation (0.15417 nm) source, equipped with a LYNXEYE super speed detector. Crystallite sizes were determined from the line broadening of the main corresponding XRD peak ($2\theta = 43.3°$) by using the Scherrer equation.

Raman spectroscopy measurements were conducted in the back-scattering configuration through an optical probe connected to Horiba Jobin-Yvon FHR640 monochromator coupled with a CCD detector. The solid-state laser (532 nm) was used as an excitation source, and the laser power was kept at ~140 W cm^{-2}. The spectral position was corrected by imposing the main peak of monocrystalline Si to 520 cm^{-1}.

Acknowledgements

The authors thank Generalitat de Catalunya for financial support through the CERCA Program, M2E (2017SGR1246), CPT (2017SGR1777) and PhD grant (M.A.) 2021DI20. IREC also acknowledges support from the European Regional Development (ERDF, FEDER) and by MCIN/AEI/10.13039/501100011033 CCU + OX (PID2019-108136RB-C33) and CERES projects (PID2020-116093RB-C42). M.C. has received her Ph.D. funding from the European Union's Horizon 2020 research and innovation programme under the Marie Skłodowska-Curie grant agreement No 754397. M.C. acknowledges her Doctorate programme, 'Programa de Doctorat en Ciència de Materials de la UAB'.

Conflict of Interest

The authors declare no conflict of interest.

Data Availability Statement

Research data are not shared.

Keywords: redox reversibility · supporting electrolyte · zinc chloride complexation · zinc-iodide flow batteries

[1] B. Li, J. Liu, Z. Nie, W. Wang, D. Reed, J. Liu, P. McGrail, V. Sprenkle, *Nano Lett.* **2016**, *16*, 4335–4340.
[2] C. Ponce de León, A. Frías-Ferrer, J. González-García, D. A. Szánto, F. C. Walsh, *J. Power Sources* **2006**, *160*, 716–732.
[3] Z. Yang, J. Zhang, M. C. W. Kintner-Meyer, X. Lu, D. Choi, J. P. Lemmon, J. Liu, *Chem. Rev.* **2011**, *111*, 3577–3613.
[4] A. Z. Weber, M. M. Mench, J. P. Meyers, P. N. Ross, J. T. Gostick, Q. Liu, *J. Appl. Electrochem.* **2011**, *41*, 1137–1164.
[5] G. L. Soloveichik, *Chem. Rev.* **2015**, *115*, 11533–11558.
[6] P. Leung, X. Li, C. Ponce de León, L. Berlouis, C. T. J. Low, F. C. Walsh, *RSC Adv.* **2012**, *2*, 10125–10156.
[7] W. Wang, Q. Luo, B. Li, X. Wei, L. Li, Z. Yang, *Adv. Funct. Mater.* **2013**, *23*, 970–986.
[8] H. Chen, T. N. Cong, W. Yang, C. Tan, Y. Li, Y. Ding, *Prog. Nat. Sci.* **2009**, *19*, 291–312.
[9] P. Alotto, M. Guarnieri, F. Moro, *Renewable Sustainable Energy Rev.* **2014**, *29*, 325–335.
[10] J. Noack, N. Roznyatovskaya, T. Herr, P. Fischer, *Angew. Chem. Int. Ed.* **2015**, *54*, 9776–9809; *Angew. Chem.* **2015**, *127*, 9912–9947.
[11] W. Wang, V. Sprenkle, *Nat. Chem.* **2016**, *8*, 204–206.
[12] Z. P. Cano, D. Banham, S. Ye, A. Hintennach, J. Lu, M. Fowler, Z. Chen, *Nat. Energy* **2018**, *3*, 279–289.
[13] P. K. Leung, C. Ponce-De-León, C. T. J. Low, A. A. Shah, F. C. Walsh, *J. Power Sources* **2011**, *196*, 5174–5185.
[14] J. Winsberg, T. Janoschka, S. Morgenstern, T. Hagemann, S. Muench, G. Hauffman, J. F. Gohy, M. D. Hager, U. S. Schubert, *Adv. Mater.* **2016**, *28*, 2238–2243.
[15] Z. Li, G. Weng, Q. Zou, G. Cong, Y. C. Lu, *Nano Energy* **2016**, *30*, 283–292.
[16] P. K. Leung, T. Matin, A. A. Shah, M. R. Mohamed, M. A. Anderson, J. Palma, *J. Power Sources* **2017**, *341*, 36–45.
[17] L. Wei, T. Zhao, L. Zeng, X. Zhou, Y. Zeng, *Energy Technol.* **2016**, *4*, 990–996.
[18] L. Wei, T. S. Zhao, G. Zhao, L. An, L. Zeng, *Appl. Energy* **2016**, *176*, 74–79.
[19] J. Vázquez-Galván, C. Flox, C. Fàbrega, E. Ventosa, A. Parra, T. Andreu, J. R. Morante, *ChemSusChem* **2017**, *10*, 2089–2098.
[20] Y. K. Zeng, X. L. Zhou, L. An, L. Wei, T. S. Zhao, *J. Power Sources* **2016**, *324*, 738–744.
[21] Y. K. Zeng, T. S. Zhao, X. L. Zhou, L. Zeng, L. Wei, *Appl. Energy* **2016**, *182*, 204–209.
[22] G. P. Rajarathnam, M. Schneider, X. Sun, A. M. Vassallo, *J. Electrochem. Soc.* **2016**, *163*, A5112–A5117.
[23] H. R. Jiang, M. C. Wu, Y. X. Ren, W. Shyy, T. S. Zhao, *Appl. Energy* **2018**, *213*, 366–374.
[24] M. C. Wu, T. S. Zhao, L. Wei, H. R. Jiang, R. H. Zhang, *J. Power Sources* **2018**, *384*, 232–239.
[25] F. C. Walsh, C. Ponce de León, L. Berlouis, G. Nikiforidis, L. F. Arenas-Martínez, D. Hodgson, D. Hall, *ChemPlusChem* **2015**, *80*, 288–311.
[26] K. Wang, P. Pei, Z. Ma, H. Chen, H. Xu, D. Chen, X. Wang, *J. Mater. Chem. A* **2015**, *3*, 22648–22655.
[27] B. Li, Z. Nie, M. Vijayakumar, G. Li, J. Liu, V. Sprenkle, W. Wang, *Nat. Commun.* **2015**, *6*, 1–8.
[28] G. M. Weng, Z. Li, G. Cong, Y. Zhou, Y. C. Lu, *Energy Environ. Sci.* **2017**, *10*, 735–741.
[29] H. Pan, B. Li, D. Mei, Z. Nie, Y. Shao, G. Li, X. S. Li, K. S. Han, K. T. Mueller, V. Sprenkle, J. Liu, *ACS Energy Lett.* **2017**, *2*, 2674–2680.
[30] C. Xie, H. Zhang, W. Xu, W. Wang, X. Li, *Angew. Chem. Int. Ed.* **2018**, *57*, 11171–11176; *Angew. Chem.* **2018**, *130*, 11341–11346.
[31] Q. P. Jian, M. C. Wu, H. R. Jiang, Y. K. Lin, T. S. Zhao, *J. Power Sources* **2021**, *484*, 229238.
[32] J. Zhang, G. Jiang, P. Xu, A. G. Kashkooli, M. Mousavi, A. Yu, Z. Chen, *Energy Environ. Sci.* **2018**, *11*, 2010–2015.
[33] C. Xie, Y. Liu, W. Lu, H. Zhang, X. Li, *Energy Environ. Sci.* **2019**, *12*, 1834–1839.
[34] S. J. Banik, R. Akolkar, *Electrochim. Acta* **2015**, *179*, 475–481.
[35] D. P. Trudgeon, K. Qiu, X. Li, T. Mallick, O. O. Taiwo, B. Chakrabarti, V. Yufit, N. P. Brandon, D. Crevillen-Garcia, A. Shah, *J. Power Sources* **2019**, *412*, 44–54.
[36] S. Hosseini, S. J. Han, A. Arponwichanop, T. Yonezawa, S. Kheawhom, *Sci. Rep.* **2018**, *8*, 1–11.
[37] F. W. Thomas Goh, Z. Liu, T. S. Andy Hor, J. Zhang, X. Ge, Y. Zong, A. Yu, W. Khoo, *J. Electrochem. Soc.* **2014**, *161*, A2080–A2086.
[38] M. Chakraborty, S. Murcia-Lopez, J. R. Morante, T. Andreu, *J. Electrochem. Soc.* **2021**, *168*, 040532.
[39] D. J. Mackinnon, J. M. Brannen, V. I. Lakshmanan, *J. Appl. Electrochem.* **1980**, *10*, 321–334.
[40] G. Trejo, R. Ortega B., Y. Meas V., P. Ozil, E. Chainet, B. Nguyen, *J. Electrochem. Soc.* **1998**, *145*, 4090–4097.
[41] K. Amini, M. D. Pritzker, *Electrochim. Acta* **2018**, *268*, 448–461.
[42] K. Ogle, S. Morel, *EUROCORR 2004 – Eur. Corros. Conf. Long Term Predict. Model. Corros.* **2004**, 1–5.
[43] W. Miao, I. S. Cole, A. K. Neufeld, S. Furman, *J. Electrochem. Soc.* **2007**, *154*, C7.
[44] S. Thomas, N. Birbilis, M. S. Venkatraman, I. S. Cole, *Corrosion* **2012**, *68*, 1–9.
[45] H. Wakita, G. Johansson, M. Sandström, P. L. Goggin, H. Ohtaki, *J. Solution Chem.* **1991**, *20*, 643–668.
[46] G. Pulletikurthi, M. S. Ghazvini, T. Cui, N. Borisenko, T. Carstens, A. Borodin, F. Endres, *Dalton Trans.* **2017**, *46*, 455–464.
[47] P. H. Svensson, L. Kloo, *Chem. Rev.* **2003**, *103*, 1649–1684.
[48] M. Mousavi, G. Jiang, J. Zhang, A. G. Kashkooli, H. Dou, C. J. Silva, Z. P. Cano, Y. Niu, A. Yu, Z. Chen, *Energy Storage Mater.* **2020**, *32*, 465–476.
[49] C. L. Bentley, A. M. Bond, A. F. Hollenkamp, P. J. Mahon, J. Zhang, *Anal. Chem.* **2016**, *88*, 1915–1921.
[50] E. R. Nightingale, *J. Phys. Chem.* **1959**, *63*, 1381–1387.
[51] D. W. Smith, *J. Chem. Educ.* **1977**, *1*, 1–3.
[52] G. Xie, T. Okada, *J. Electrochem. Soc.* **1995**, *142*, 3057–3062.
[53] A. Goswami, A. Acharya, A. K. Pandey, *J. Phys. Chem. B* **2001**, *105*, 9196–9201.
[54] S. Ito, M. Sugimasa, Y. Toshimitsu, A. Orita, M. Kitagawa, M. Sakai, *Electrochim. Acta* **2019** *319*, 164–174.

Manuscript received: April 8, 2023
Accepted manuscript online: April 10, 2023
Version of record online: April 21, 2023